Shift-current response as a probe of quantum geometry and electron-electron interactions in twisted bilayer graphene

Swati Chaudhary,[1,2,3,4,5,*,†] Cyprian Lewandowski,[1,2,*,‡] and Gil Refael[1,2]

[1]*Department of Physics, California Institute of Technology, Pasadena, California 91125, USA*
[2]*Institute for Quantum Information and Matter, California Institute of Technology, Pasadena, California 91125, USA*
[3]*Department of Physics, The University of Texas at Austin, Austin, Texas 78712, USA*
[4]*Department of Physics, Northeastern University, Boston, Massachusetts 02115, USA*
[5]*Department of Physics, Massachusetts Institute of Technology, Cambridge, Massachusetts 02139, USA*

(Received 2 August 2021; revised 10 January 2022; accepted 27 January 2022; published 28 February 2022)

Moiré materials, and in particular twisted bilayer graphene (TBG), exhibit a range of fascinating phenomena that emerge from the interplay of band topology and interactions. We show that the nonlinear second-order photoresponse is an appealing probe of this rich interplay. A dominant part of the photoresponse is the shift current, which is determined by the geometry of the electronic wave functions and carrier properties and thus becomes strongly modified by electron-electron interactions. We analyze its dependence on the twist angle and doping and investigate the role of interactions. In the absence of interactions, the response of the system is dictated by two energy scales: (i) the mean energy of direct transitions between the hole and electron flat bands and (ii) the gap between flat and dispersive bands. Including electron-electron interactions both enhances the response at the noninteracting characteristic frequencies and produces new resonances. We attribute these changes to the filling-dependent band renormalization in TBG. Our results highlight the connection between nontrivial geometric properties of TBG and its optical response, as well as demonstrate how optical probes can access the role of interactions in moiré materials.

DOI: 10.1103/PhysRevResearch.4.013164

I. INTRODUCTION

Twisted bilayer graphene (TBG) is an exciting arena where quantum geometry and enhanced electronic interactions play both against and with each other. While the interactions are boosted by the flatness of the electronic bands near charge neutrality, geometric effects are amplified by the large size of the moiré unit cell as the lattice constant sets the scale for the Berry connection. This conjunction of interactions and geometry is responsible for a growing list of fascinating effects [1–9] ranging from surprisingly strong superconductivity [5–7] to symmetry-breaking electronic transitions ("cascade") [8,9] and anomalous Hall phases [3]. In this paper we focus on the second-order photoresponse of TBG, in particular, on the shift current. We contend that it is a unique probe that can wield the enhanced geometric effects of the electronic wave function to systematically probe the role of interactions in TBG at a range of fillings and twist angles.

By quantum geometry (QG) we refer to the structure of the electronic Bloch wave functions. Many interesting signatures of QG are revealed in transport properties and optical responses of these systems [10–20], and especially in the zero-magnetic field quantized anomalous linear Hall effect in setups with time-reversal symmetry (TRS) [3,4,21]. The effects of QG go well beyond linear response effects, and can in fact manifest themselves in nonlinear optical responses (NLORs) as shown recently [22–37]. Furthermore, the NLOR does not require broken TRS, but rather a nonzero Berry curvature profile. These nonlinear effects can manifest in various ways, such as nonlinear response to dc fields (induced by Berry curvature dipole [22,26,27,33–37]), second-harmonic generation (SHG), bulk-photovoltaic effects such as shift current (SC) [28,29,31,38], and circular photogalvanic effects (CPGEs) [24,39,40]. Recently, there has been a lot of emphasis on the nonlinear response to ac fields [23,24,40], which not only serves as a probe of nontrivial topology but also heralds the promise of more efficient and robust photovoltaic devices [32].

The shift-current response [41–44] is a particularly interesting part of the NLOR. In topological systems it could generate a giant dc response from weak linearly polarized electromagnetic fields, which makes it relevant for photovoltaic applications [28–32]. Furthermore, the shift-current response is tied to the quantum geometric properties of the system [11,12,15,45] and microscopically arises due to a change in properties of the Bloch wave function upon excitation between bands. Specifically, the magnitude of such

*These authors contributed equally to this work.
†swati.chaudhary@austin.utexas.edu
‡cyprian@caltech.edu

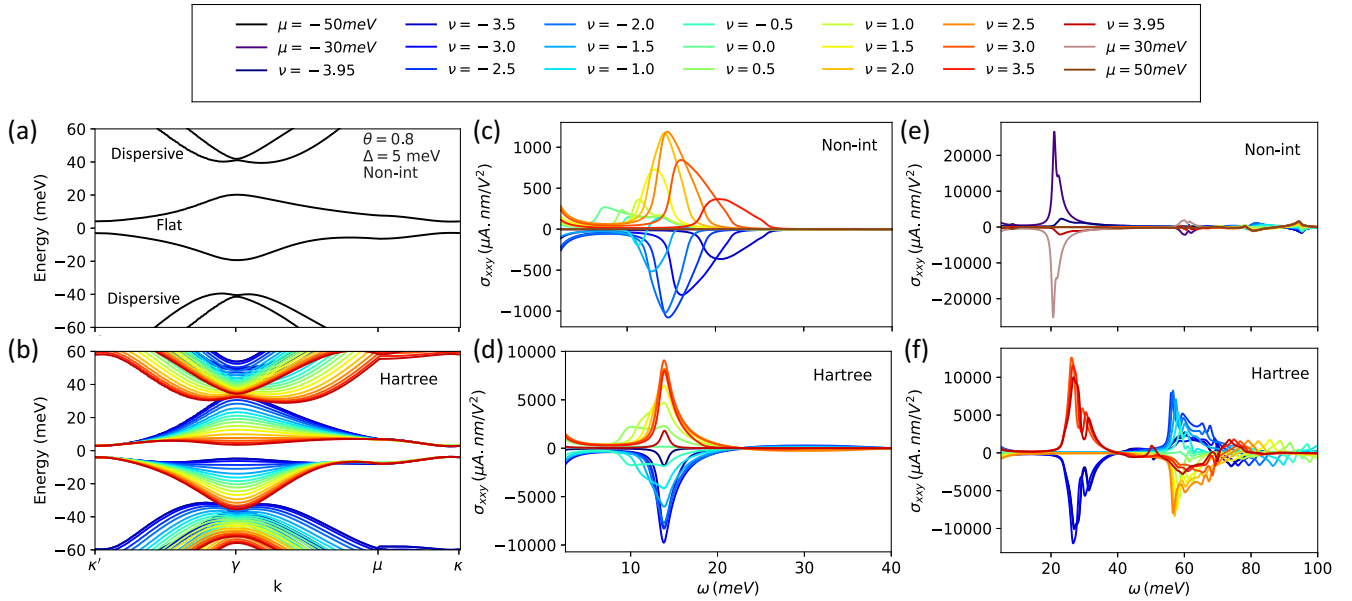

FIG. 1. Interaction-induced modifications to band structure and shift-current response of twisted bilayer graphene. (a) Band structure of the noninteracting (Non-int) model presented in Eq. (2), (b) band structure that includes Hartree corrections at different fillings ν, (c) and (d) contributions to the second-order conductivity $\sigma^{y}_{xx}(0, \omega, -\omega)$ from flat-to-flat band transitions for the noninteracting case and for the interacting case with Hartree corrections, and (e) and (f) contributions to the second-order conductivity $\sigma^{y}_{xx}(0, \omega, -\omega)$ from flat-to-dispersive band transitions for the noninteracting case and for the interacting case with Hartree corrections. These Hartree corrections flatten both the flat and dispersive bands significantly as the filling is increased. This results in an enhanced second-order response and also gives rise to a second peak in the flat-to-dispersive contribution. As a consequence of a velocity gauge, as explained in the text, there is an apparent $\propto 1/\omega^2$ divergence as $\omega \to 0$.

QG effects is sensitive to the change in average position of Bloch wave functions within the unit cell [15]. Previous works that studied the shift-current response in bilayer graphene and transition-metal dichalcogenides (TMDs) [32,46–49] predicted a strong effect due to their nonzero Berry curvature profile.

Quantum-geometry-induced processes become more dominant in flat bands [16,50], where the large effective lattice constant sets the scale for the Berry connection in the flat bands. Recent pioneering studies considered twisted bilayer graphene at the magic angle (MATBG) [51,52] and confirmed the expectation of an unprecedented magnitude of the response.

Our work expands on these initial investigations and provides a systematic study of the relationship of the shift-current response to twist angle, filling factor, and encapsulation environment. We identify the role of the band structure, relevant quantum geometry tensor elements, and the system's symmetries in determining the shift-current response. Particularly, we compute the shift-current response while including electron-electron interactions and show that they significantly enhance the response as compared with a noninteracting model. Many recent works [53–62] have shown that interactions can also drastically alter the noninteracting band structure and associated wave-function profiles. As we will show in this paper, these modifications significantly affect the shift-current response studied in previous works [51,52] that only considered a response of a noninteracting TBG.

Inspired by recent experimental results [61,63], we consider a specific class of electron-electron renormalizations of the electron band structure that stem from inhomogeneous charge distribution in the moiré unit cell (see Figs. 1(a) and 1(b) and Refs. [53,54,57]). We demonstrate that these interactions can change both the magnitude and frequency response of the second-order conductivity. We argue that these changes arise from the interaction-induced band flattening and modifications of Bloch wave functions, specifically the quantum geometric connection, that are closely related to the shift-current photoresponse [12,15].

For simplicity, we perform our self-consistent calculations using temperature $T = 0$ K, but we expect the observed features to remain prominent up to liquid nitrogen temperatures, $T \approx 77$ K. This is because the characteristic energy scale for flat-to-dispersive band transitions that produces new resonances as well as the charge-inhomogeneity-driven band flattening is above that energy scale. Also, since we are concerned with this high-temperature regime, we do not consider correlated effects that typically emerge at temperatures $T \lesssim 15$ K [1,5,8,64].

In addition to the shift current, quantum geometry can also lead to other nonlinear optical responses such as injection current [24,39,40], which arises from the change in group velocity of carriers upon excitation between two bands. However, for time-reversal-symmetric systems, such effects vanish for linearly polarized light [12], and thus we ignore these effects in this paper. Additionally, at frequencies much smaller than the gap, there can be a semiclassical contribution

to second-order conductivity arising from the Berry curvature dipole [26,27,29,65]. In two-dimensional (2D) systems, this contribution survives only if the largest symmetry is a single mirror plane [27], which is not the case for TBG.

The paper is organized as follows. In Sec. II we present a brief summary of our main results. In Sec. III we present the model used in our simulations, the mean-field treatment of Coulomb interactions, and the methods employed to evaluate the shift-current response. We also compare different approaches used in the literature and comment on their numerical amenability. In Sec. IV we proceed to study the shift-current response in a noninteracting twisted bilayer model and investigate the role of twist angle, sublattice offset, and symmetry properties. Additionally, we analyze the contribution arising from different types of band transitions, e.g., flat-to-flat (FF) and flat-to-dispersive (FD) bands. In Sec. V we discuss how these results are modified by interactions. Finally, we conclude by providing a summary of our analysis and specific experimental predictions.

II. SUMMARY OF RESULTS

We study the role of twist angle, doping, encapsulation environment, and electron-electron interactions in the shift-current response in twisted bilayer graphene. We find that in the absence of interactions, or equivalently at twist angles where the noninteracting band structure accurately captures electronic properties, the photoresponse has a universal form. This form is controlled by a moiré length scale and characteristic energies associated with flat-to-flat and flat-to-dispersive band transitions. The overall contribution of these two—flat-to-flat and flat-to-dispersive—processes to the shift current also depends on the sublattice offset, which can be tuned by varying the encapsulation environment. A finite sublattice offset leads to a gap opening between flat bands which can be controlled by the relative alignment between the graphene and hexagonal boron nitride (hBN) layer. Specifically, we find that the sublattice offset does not drastically affect the gap between the flat and dispersive bands, unlike the gap between the flat bands. Therefore the sublattice offset allows one to control the relative importance of both types of transitions in shaping the photoresponse.

Most importantly, we find that electron-electron interactions significantly change the shift-current response as compared with a noninteracting system [see Figs. 1(c)–1(f)]. The role of interactions in the photoresponse becomes more pronounced as the twist angle is brought closer to the magic angle, leading, within the extent of approximations used for the modeling of interactions, to a sharp increase in magnitude and narrowing of corresponding frequency window where resonances in shift current were expected on the basis of the noninteracting model. The key contribution of electron-electron interactions to the shift current is in altering the photoresponse corresponding to transitions between flat and dispersive bands. We attribute these features to electron-electron-interaction-driven changes to the band dispersion, the nature of Bloch wave functions, and thus the resulting quantum geometry.

Our results demonstrate that frequency range and magnitude can be tuned significantly by varying the twist angle and the substrate properties. Specifically, we observe a second-order conductivity of the order of 1000 μA nm V^{-2} in the frequency range of 10–100 meV. This is in agreement with previous results of Refs. [51] and [46] for TBG and gapped bilayer graphene, respectively. We note, however, that Ref. [51] studies the frequency response in the range 1–10 meV and Ref. [46] considers a frequency of 100 meV. Finally, our work shows how the photoresponse can serve as a probe of electron-electron interactions in TBG, pointing towards a possible experimental direction for the TBG field.

III. MODEL AND METHODS

A. TBG single-particle Hamiltonian

The single-particle energy spectrum of twisted bilayer graphene near the magic angle can be described with the help of a continuum model [66–69]. Here, we follow the notation and model considered in Ref. [66], which gives a Hamiltonian:

$$\mathcal{H}_0 = \sum_{\gamma=\{\zeta,\sigma\}} \int_\Omega d^2\mathbf{r}\, \psi_\gamma^\dagger(\mathbf{r}) \widehat{\mathbf{H}}^{(\zeta,\sigma)} \psi_\gamma(\mathbf{r}), \tag{1}$$

$$\widehat{\mathbf{H}}^{(\zeta,\sigma)} = \begin{pmatrix} H_{\zeta 1}(\mathbf{r}) & U_\zeta^\dagger(\mathbf{r}) \\ U_\zeta(\mathbf{r}) & H_{\zeta 2}(\mathbf{r}) \end{pmatrix}, \tag{2}$$

where Ω represents the moiré unit cell, $H_{\zeta,l}$ represents the intralayer Hamiltonian of layer $l = 1, 2$, and $U_\zeta(\mathbf{r})$ encodes the moiré interlayer hopping. The Hamiltonian is written in the basis of (A_1, B_1, A_2, B_2) sites of the two layers, and we use the shorthand notation $\gamma \equiv \{\zeta(=\pm 1), \sigma(=\pm 1)\}$ for the valley and spin degrees of freedom, respectively. In the rest of this paper, we refer to this Hamiltonian as the "noninteracting model."

The intralayer part of the Hamiltonian $H_{\zeta,l}$ is given by the two-dimensional Dirac equation expanded about the $\mathbf{K}_\zeta^l$ point of the original graphene layer,

$$H_l = -\hbar v \left[R(\pm\theta/2)\left(\mathbf{k} - \mathbf{K}_\zeta^l\right)\right] \cdot (\zeta\sigma_x, \sigma_y) + \Delta_l \sigma_z, \tag{3}$$

where $\mathbf{k}$ is a momentum in the Brillouin zone (BZ) of the original graphene layers, $R(\pm\theta/2)$ is the 2×2 two-dimensional matrix accounting for the rotation of layer $l = 1(2)$ by an angle $\pm\theta/2$ about the z axis with respect to the initial AA stacked bilayer. We set $\hbar v/a = 2.1354$ eV as the kinetic energy scale for the Hamiltonians, $H_{\xi l}$ with $a = 0.246$ nm being the original graphene's lattice constant. We also introduce a layer-dependent sublattice offset term, $\Delta_l \sigma_z$, that leads to a gap opening at the Dirac points and breaking of inversion symmetry.

The moiré interlayer potential $U_\zeta(\mathbf{r})$ in Eq. (2) can be approximated as

$$U_\zeta(\mathbf{r}) = \begin{pmatrix} u & u' \\ u' & u \end{pmatrix} + \begin{pmatrix} u & u'e^{-i2\pi\zeta/3} \\ u'e^{i2\pi\zeta/3} & u \end{pmatrix} e^{i\zeta \mathbf{G}_1^M \cdot \mathbf{r}} + \begin{pmatrix} u & u'e^{i2\pi\zeta/3} \\ u'e^{-i2\pi\zeta/3} & u \end{pmatrix} e^{i\zeta(\mathbf{G}_1^M + \mathbf{G}_2^M)\cdot\mathbf{r}}, \tag{4}$$

where we take $u' = 90$ meV and $u = 0.4u'$ for twist angles near the magic angle. We justify our choice of parameters in the next section. To diagonalize the Hamiltonian equation (2) in $\mathbf{k}$ space, we can account for this interlayer potential by

introducing a coupling between Bloch wave *Ansätze* at momentum $\mathbf{k}$ and $\mathbf{k}+\mathbf{G}$. Here, $\mathbf{G} = n_1\mathbf{G}_1^M + n_2\mathbf{G}_2^M$ is a linear combination of moiré reciprocal vectors $\mathbf{G}_1^M$ and $\mathbf{G}_2^M$, where n_1 and n_2 are integers, and $G = |\mathbf{G}_1^M| = |\mathbf{G}_2^M|$ sets the characteristic momentum scale of the problem. These reciprocal lattice vectors are given by $\mathbf{G}_i^M = R(-\theta/2)\mathbf{G}_i - R(\theta/2)\mathbf{G}_i$, with $\mathbf{G}_1 = (2\pi/a)(1, -1/\sqrt{3})$ and $\mathbf{G}_2 = (2\pi/a)(0, 2/\sqrt{3})$ being the reciprocal lattice vectors of a graphene monolayer.

B. Mean-field interacting Hamiltonian

We consider electron-electron interactions given by the Coulomb term

$$\mathcal{H}_c = \frac{1}{2}\int_\Omega d^2\mathbf{r}d^2\mathbf{r}'\delta\rho(\mathbf{r})\mathcal{V}_c(\mathbf{r}-\mathbf{r}')\delta\rho(\mathbf{r}'), \tag{5}$$

$$\delta\rho(\mathbf{r}) = \sum_{\gamma=\{\zeta,\sigma\}} \psi_\gamma^\dagger(\mathbf{r})\psi_\gamma(\mathbf{r}) - \rho_{\mathrm{CN}}(\mathbf{r}), \tag{6}$$

where $\delta\rho(\mathbf{r})$ is the density relative to that at charge neutrality, $\rho_{\mathrm{CN}}(\mathbf{r})$, and $\mathcal{V}_c(\mathbf{r}-\mathbf{r}')$ is the Coulomb potential with a Fourier transform, $\mathcal{V}_c(\mathbf{q}) = 2\pi e^2/\varepsilon q$. The dielectric constant ε depends on the substrate and is treated as a free parameter (reasons to be made clear below). We approximate the above interaction term using a self-consistent Hartree approximation $\mathcal{H}_c \approx \mathcal{H}_H$, where

$$\mathcal{H}_H = \sum_{\gamma=\{\zeta,\sigma\}}\int_\Omega d^2\mathbf{r}V_H(\mathbf{r})\psi_\gamma^\dagger(\mathbf{r})\psi_\gamma(\mathbf{r}) \tag{7}$$

with the Hartree potential

$$V_H(\mathbf{r}) = \int_\Omega d^2\mathbf{r}'\mathcal{V}_C(\mathbf{r}-\mathbf{r}')\sum_\gamma \langle\psi_\gamma^\dagger(\mathbf{r}')\psi_\gamma(\mathbf{r}')\rangle_H. \tag{8}$$

In the above expression, $\langle\cdots\rangle_H$ denotes a summation over occupied states measured from the charge neutrality point (CNP; $\nu = 0$) [53]. When doping is increased with respect to the charge neutrality point, there is a preferential buildup of charge at *AA* sites in real space [53], corresponding to electronic states near the κ, κ' points of the mini Brillouin zone. The nonuniform spatial charge distribution generates an electrostatic potential that prefers an even redistribution of the electron density. In contrast, the real-space charge distribution corresponding to electronic states near the γ point is more uniform in the unit cell. The effect of the electrostatic Hartree potential and the associated charge redistribution thus leads to an increase in the energy of the electronic states near the κ, κ' and μ points compared with the energy of states near the γ point [53,54,57,70,71].

The effect of the Hartree potential becomes increasingly pronounced as a function of decreasing twist angle, especially near the magic angle, where the noninteracting bandwidth is minimal. There is an increasing tendency towards band inversion near the γ point [54,55], a feature that has not been observed in experiments to date [61]. However, it is important to note that other mechanisms, for example, strain or a Fock term, can act against this tendency towards band inversion by increasing the overall bandwidth (both strain and Fock) or by contributing an opposing correction to the self-energy as compared with the Hartree term (Eq. (8); Fock only). In our analysis we focus only on the Hartree correction for a wide range of θ and caution that results in the vicinity of the magic angle, $0.96^\circ < \theta < 1.04^\circ$ in our parametrization, would likely be modified by other interaction effects. More specifically, in this range, we anticipate that the Hartree term would produce extreme band inversions not seen experimentally, which are most likely counteracted by another mechanism.

The band structure is obtained by employing a fitting procedure introduced in Ref. [61] and summarized in Appendix A of the Supplemental Material [72]. This approximate fitting protocol relies on matching microscopic parameters of the Hamiltonian such that the theoretical energy spectrum of the system reproduces experimental scanning tunneling microscopy (STM) results sufficiently far away from the magic angle where no correlated effects are present. As explained in the Supplemental Material [72] and Ref. [61], for general agreement with the experimental results, it is necessary to use a dielectric constant ε larger than that set by the substrate. Similar procedures were employed in earlier studies [53,55,73], and their origins theoretically can be justified by arguing that dispersive bands renormalize the dielectric constant for the Coulomb interaction projected to the flat bands. The final renormalized band structures at fixed angle of $\theta = 0.8^\circ$ are shown as a function of filling ν per moiré unit cell in Fig. 1(b). The most notable manifestation of the Hartree-induced effects is the band flattening around the γ and μ points beyond a certain filling.

We note that the contribution of band-flattening effects to TBG properties was studied in recent works [74–76]. Qualitatively, the role of band flattening was either to enhance the density of states at the Fermi level or to decrease overall bandwidth, and as a result, the corresponding twist angle range, over which correlated effects were expected, increased. We stress, however, that no other papers that studied NLORs in TBG [51,52] have considered the role that interactions can play in the photoresponse.

Before proceeding with the discussion of the shift currents in TBG, we pause to clarify key assumptions of our modeling. Firstly, we intentionally do not include the effects associated with the "cascade" transitions at integer fillings near the magic angle [8,9] and the correlated effects such as superconductivity [5] or insulating states [1]. Physically, this approximation is motivated by the fact that optical NLOR experiments are typically performed at temperatures [23] exceeding the characteristic temperatures ($T \lesssim 15$ K) associated with these phenomena [1,5,8,64]. In principle, however, these effects could provide interesting constraints on and signatures in the photoresponse. We expect Hartree corrections to persist to higher temperatures as they are a reflection of charge inhomogeneity of the system. Secondly, we also neglect the possibility of varying interlayer hopping parameters (u, u') in Eq. (4). We argue that this approximation is justified since our choice of $u' = 90$ meV is comparable to typical literature values and the ratio of $\eta = u/u = 0.4$ is not too far from values quoted in the literature that are typically in the range $\eta = 0.3$–0.7. Most crucially, however, even if η were to be varied with the twist angle, the location of the van Hove singularity would remain fixed near filling of ± 1.9 (or not drastically different energies; see also Ref. [77]) until very high η values of 0.8. Such values are typically not used in modeling. As such we expect that although quantitative changes (such as precise

frequency locations of peaks) can vary, overall behavior of the system, in particular, its charge density profile, will remain qualitatively similar.

C. Shift current

The shift current is a second-order dc response to an electromagnetic field arising from interband optical excitations [41]. In time-reversal-symmetric systems, the shift current depends on the linearly polarized component of light, and its origins can be traced back to the real-space shift experienced by the Bloch wave packet upon excitation from one band to another. If the light is circularly polarized, then band transitions can also lead to an additional second-order dc response, known as injection current, which arises due to the change in carrier velocities upon excitation [43]. However, for a linearly polarized light, this kind of injection current response vanishes in a two-dimensional system if the time-reversal symmetry is preserved in the system. The shift current is sensitive to the intraband and interband Berry connection of the bands involved in the transition process [43] and hence offers a possibility to detect and harness the nontrivial band topology of Bloch bands in photovoltaic processes.

The shift-current response is determined by a rank-three tensor, $\sigma^{\mu}_{\alpha\alpha}$, which satisfies

$$\mathbf{J}^{\mu} = 2\sigma^{\mu}_{\alpha\alpha}(0, \omega, -\omega)\mathcal{E}^{\alpha}(\omega)\mathcal{E}^{\alpha}(-\omega), \tag{9}$$

where $\mathbf{J}^{\mu}$ is the μth component of the current density, $\boldsymbol{\mathcal{E}}(t) = \boldsymbol{\mathcal{E}}(\omega)e^{i\omega t} + \boldsymbol{\mathcal{E}}(-\omega)e^{-i\omega t}$ is the electric field, and Greek indices denote spatial components, $\alpha = \{x, y\}$. The second-order conductivity tensor element, $\sigma^{\mu}_{\alpha\alpha}(0, \omega, -\omega)$, is given by (see Appendix B of the Supplemental Material [72] and Ref. [78])

$$\sigma^{\mu}_{\alpha\alpha}(0, \omega, -\omega) = \frac{\pi e^3}{\hbar^2}\sum_{m,n}\int d^2\mathbf{k} f_{mn}\left|\mathbf{A}^{\alpha}_{mn}\right|^2\mathbf{S}^{\mu\alpha}_{mn}\delta(\omega - \varepsilon_{mn}), \tag{10}$$

where $\varepsilon_{mn} = \varepsilon_m - \varepsilon_n$ is the energy difference between the two states that participate in the optical transition and $f_{mn} = f_m - f_n$ is the difference in occupancy of their energy levels. The above expression features two geometric terms: a shift vector $\mathbf{S}^{\mu\alpha}_{mn} = \mathbf{A}^{\mu}_{mm} - \mathbf{A}^{\mu}_{nn} - \partial_{\mu}(\mathrm{Arg}\mathbf{A}^{\alpha}_{mn})$ and the interband Berry connection $\mathbf{A}_{mn} = -i\langle u_m|\nabla_{\mathbf{k}}|u_n\rangle$ for Bloch wave functions $|u_m\rangle$ and $|u_m\rangle$. This interband Berry connection enters into the shift-vector expression as the electromagnetic (EM) field couples through the dipole matrix and carries no other direct physical interpretation, while the shift vector represents the shift experienced by the Bloch wave packet upon excitation from the mth to the nth band [42,44,78]. We denote the integrand of the above expression as $R^{\alpha\alpha\mu}_{mn} = |\mathbf{A}^{\alpha}_{mn}|^2\mathbf{S}^{\mu\alpha}_{mn}$, and provided that the Hamiltonian has a linear dependence on momentum, it can also be expressed as

$$R^{\alpha\alpha\mu}_{ab} = \frac{1}{\varepsilon^2_{ab}}\mathrm{Im}\left[\frac{h^{\alpha}_{ab}h^{\mu}_{ba}\Delta^{\alpha}_{ab}}{\varepsilon_{ab}}\right] + \frac{1}{\varepsilon^2_{ab}}\mathrm{Im}\left[\sum_{d\neq a,b}\left(\frac{h^{\alpha}_{ba}h^{\mu}_{ad}h^{\alpha}_{db}}{\varepsilon_{ad}} - \frac{h^{\alpha}_{ba}h^{\mu}_{db}h^{\alpha}_{ad}}{\varepsilon_{db}}\right)\right], \tag{11}$$

where $h^{\alpha}_{ab} = \langle a|\nabla_{k_\alpha}H|b\rangle$ and $\Delta^{\alpha}_{ab} = h^{\alpha}_{aa} - h^{\alpha}_{bb}$. The above expression for the shift current is equivalent to the sum rule commonly used to calculate the shift vector [78]. We stress that if the time-reversal symmetry is broken intrinsically or by application of circularly polarized light, there can be an additional contribution to the current density which is linear in scattering time and is known as the injection current [24,39,40,43].

In the literature there are several methods to calculate second-order NLOR conductivity [32,43,79,80]. In fact, in some previous works, Eq. (10) is often presented in a slightly different form without any explicit reference to the shift vector. For example, one of the most common expressions [52,80] is of the form

$$\sigma^{\mu}_{\alpha\beta} = -\frac{e^3}{\hbar^2\omega^2} \times \mathrm{Re}\left(\sum_{\Omega=\pm\omega,m,n,l}\int d^2\mathbf{k}\frac{h^{\alpha}_{nl}h^{\beta}_{lm}h^{\mu}_{mn}}{(\varepsilon_{mn} - i0^+)(\varepsilon_{nl} + \Omega - i0^+)}\right), \tag{12}$$

which we show in Appendix B of the Supplemental Material [72] is equivalent to Eq. (10) except for the injection current term which arises for $m = n$ in the above summation. This injection current term vanishes if $\alpha = \beta$ or if the TRS is preserved. We also note an apparent discrepancy between the two expressions. The above expression incorporates three states involved in the transition process, while the expression of Eq. (10) features only two. This is resolved by realizing that one of the states in the above expression comes from a virtual transition and is accounted for explicitly in the summation as shown in Eq. (11). Also, we caution that this expression is derived by employing the velocity gauge. This gauge is more suitable for calculating optical responses when the matrix elements of $\nabla_{\mathbf{k}}H$ are known, which is the case here. However, it is also well known that it suffers from some apparent divergences, $\propto 1/\omega^2$ in the limit $\omega \to 0$, and hence cannot predict the response at $\omega \ll \varepsilon_{mn}$ [79].

The above shift-vector expression of Eq. (10) can be calculated directly from the Berry connection matrix. In practice, however, the direct numerical approach is plagued by gauge fixing issues and hence is not reliable. We instead consider the approach used in Refs. [32,79] to calculate the shift vector using the sum rule described in Eq. (11), which, as explained above, is equivalent to the three-velocity expression in Ref. [79]. This approach is more amenable for numerical simulations and also puts the different expressions considered above on an equal footing. We provide a detailed derivation of the shift-current conductivity in Appendix B of the Supplemental Material [72] and elucidate the connection between different expressions encountered in the literature.

D. Symmetry constraints on second-order conductivity

It is well known that second-order optical processes are observed only in noncentrosymmetric materials [44,81]. The number of nonvanishing and independent elements of the second-order conductivity tensor can be deduced directly from the symmetry groups of the crystal via a simple application of group theory. The continuum TBG model considered here has D_3 symmetry generated by a C_{3z} and C_{2y} when the

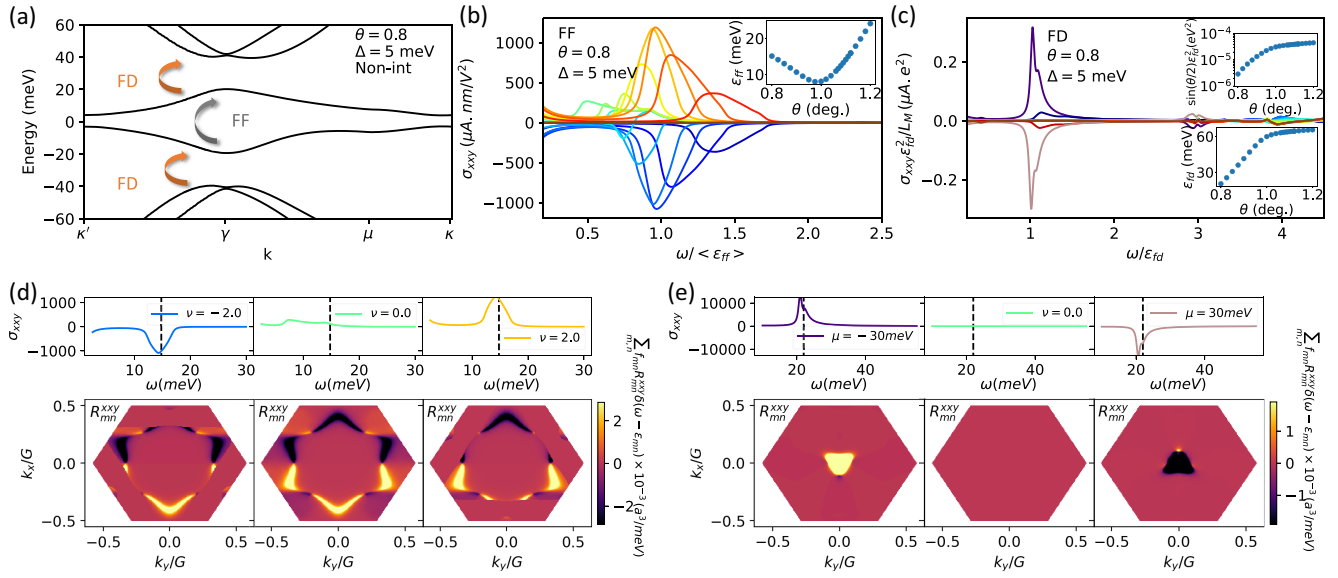

FIG. 2. Band structure and shift-current response of twisted bilayer graphene near the magic angle. (a) Band structure of noninteracting twisted bilayer graphene for a twist angle $\theta = 0.8^\circ$ and a sublattice offset $\Delta = 5$ meV on both layers. Here, FF and FD denote flat-to-flat and flat-to-dispersive band transitions, respectively. (b) FF contribution to second-order conductivity as a function of frequency shown in units of average gap between two flat bands. The behavior of this average gap with twist angle θ is shown in the inset. Note that the van Hove singularity in our model occurs near $\nu \approx \pm 1.9$ and thus the peak value of σ_{xxy} is significantly larger for fillings close to this value. (c) FD contribution to shift-current conductivity scaled by ε_{fd}^2/L_M (see main text for justification) as a function of frequency in units of the band gap between flat and dispersive bands denoted by ε_{fd}. Dependence of this energy gap ε_{fd} and the moiré-length-dependent parameter ε_{fd}^2/L_M is shown in the insets. Here the same filling to color assignment is made as in Fig. 1. (d) and (e) The top row shows the conductivity at different fillings, and the bottom row shows the k-space profile of the integrand $\sum_{m,n} f_{mn} R^{xxy}_{mn} \delta(\omega - \varepsilon_{mn})$ contributing to the second-order conductivity at the frequency corresponding to the dashed line for flat-to-flat and flat-to-dispersive transitions shown in the top row, respectively.

sublattice offset term is the same on both layers. However, when $\Delta_1 \neq \Delta_2 \neq 0$, the symmetry group reduces to C_{3z}. As a result of these symmetry properties, as derived in Appendix C of the Supplemental Material [72], we expect the conductivity tensor to satisfy

$$\sigma^y_{xx} = -\sigma^y_{yy} = \sigma^y_{xy} = \sigma^x_{yx} \neq 0,$$
$$\sigma^x_{yy} = -\sigma^x_{xx} = \sigma^y_{yx} = \sigma^y_{xy} = 0 \tag{13}$$

when $\Delta_1 = \Delta_2 \neq 0$. On the other hand, for $\Delta_1 \neq \Delta_2$, we have

$$\sigma^y_{xx} = -\sigma^y_{yy} = \sigma^y_{xy} = \sigma^x_{yx} \neq 0,$$
$$\sigma^x_{yy} = -\sigma^x_{xx} = \sigma^y_{yx} = \sigma^y_{xy} \neq 0. \tag{14}$$

Indeed these group-theory-based conclusions can be explicitly checked through evaluation of Eq. (10). When $\Delta_1 = \Delta_2 = 0$ inversion symmetry is unbroken and the conductivity tensor vanishes.

IV. SHIFT CURRENT IN THE NONINTERACTING CASE

In this section, we investigate how this shift current changes with different parameters of the system, for now in the absence of electron-electron interaction. We identify two different contributions to the photocurrent in the presence of linearly polarized light: (i) those originating from transitions from a flat band to another flat band, which is referred to as the FF contribution, and (ii) those arising due to transitions between a flat band and a dispersive band, which is referred to as the FD contribution. Both are schematically depicted in Fig. 2(a), where we have explicitly summed up the contribution from two valleys.

The frequency dependence of the second-order conductivity is dictated by the integrand $\sum_{m,n} f_{mn} R^{\alpha\alpha\mu}_{mn} \delta(\omega - \varepsilon_{mn})$. For the cases of flat-to-flat transitions, as expected, the peak frequency is close to the average gap between two flat bands as shown in Fig. 2(b), and the obtained second-order conductivity looks almost identical for all twist angles away from the magic angle. This result is to be expected as the TBG continuum model (near the magic angle) for various θ produces qualitatively similar band structures (and wave functions) up to an overall scale factor. Furthermore, the peak of the response in Fig. 2(b) occurs near $\nu \approx 2$, which corresponds to the filling associated with the van Hove singularity location $\nu \approx 1.9$ for our continuum model parameters (cf. Supplemental Material Fig. S1 for a chemical level assignment for each filling). As the (u, u') parameters of Eq. (2) are kept constant for all θ, this location of the van Hove singularity will remain at the same filling, further demonstrating the similarity of the response for a wide range of angles.

In addition to being sensitive to the energy gap between flat bands, the overall behavior of second-order conductivity also depends on the k-space profile of the quantity $\sum_{m,n} f_{mn} R^{\alpha\alpha\mu}_{mn} \delta(\omega - \varepsilon_{mn})$, which we refer to as the shift-vector integrand. An important point to notice is that the profile of the shift-vector integrand, $R^{\alpha\alpha\mu}_{mn}$, in momentum space peaks around the μ points and has equal regions of positive and negative values as shown in the middle panel of Fig. 2(d). However, the integral in Eq. (10) also has a

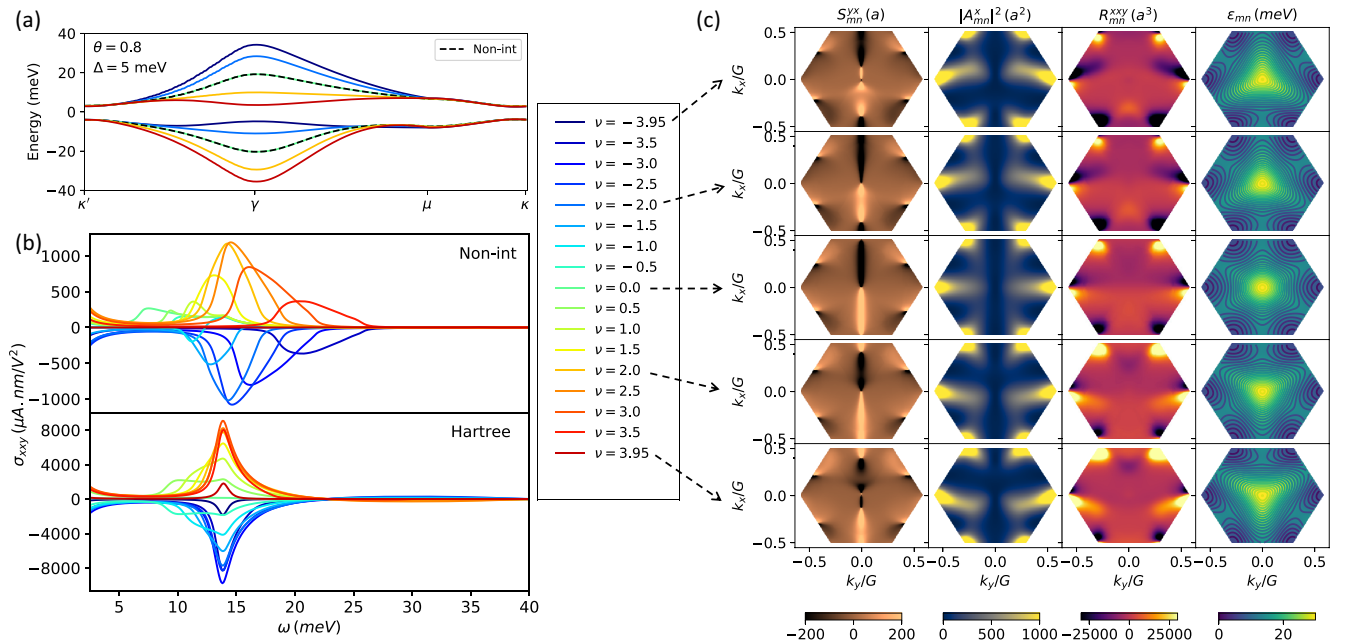

FIG. 3. Interaction-induced modifications of band structure, second-order conductivity, shift vector, and interband Berry connection for flat-to-flat band transitions. (a) Band structure with Hartree corrections. All curves are shifted to the same energy at κ'. Note how as filling increases (decreases), the electron (hole) flat band flattens and the hole (electron) band broadens. (b) FF contribution to shift-current conductivity for the noninteracting case (upper panel) and the interacting case (bottom panel). Electron-electron band flattening increases the overall magnitude of the response and narrows the resonance in frequency. (c) k-space profiles of the shift vector S^{yx}_{mn} in units of the lattice constant of the monolayer graphene lattice, interband Berry connection magnitude square, $|A^{x}_{mn}|^2$, the integrand R^{xxy}_{mn}, and energy contours for ε_{fd} in k space for the transition between two flat bands at four different fillings used to calculate shift-current response in Eq. (10). It is worth noticing that the shift vector can be orders of magnitude larger than the lattice constant a. This is expected as the Berry connection is roughly of the order of the lattice constant of the moiré lattice.

$\delta(\omega - \varepsilon_{mn})$ factor, and the energy contours for a given valley are not symmetric about $k_x = 0$, which results in a large net contribution whenever the filling is nonzero as shown in Fig. 2(d) (left and right panels). This imbalance between positive and negative regions is more prominent for the fillings $\nu \approx 2$, which results in a significant contribution from the regions near the μ point (see later discussion surrounding Fig. 5). It is worth noticing that these regions are extremely flat (as they lie in the vicinity of the van Hove singularity) and thus contribute heavily due to the large density of states. The shift vector from the $\zeta = -1$ valley is opposite in value to the shift vector from the $\zeta = +1$ valley, but at the same time the energy contours are time-reversal partners of each other, which results in the same contribution to second-order conductivity. We can apply similar arguments to conclude that the contribution from shift vector integrand R^{yyx} would vanish as the energy contours are symmetric about $k_y = 0$ but $R^{yyx}(k_x, k_y) = -R^{yyx}(k_x, -k_y)$. This is to be expected from the symmetry analysis of Sec. III D, but here it is demonstrated as an explicit consequence of the integrand $R^{\alpha\alpha\mu}$.

In fact, the frequency dependence of the photoresponse for the noninteracting model is largely decided by the gap, which can be tuned by improving the lattice alignment between between the hBN layers and the TBG sample. In our plots we considered a sublattice offset $\Delta = 5$ meV for both layers, which results in a gap of about 10 meV, and thus the contribution from flat-to-flat band transitions peaks around 10 meV. We present our results for other sublattice offset values in Fig. S2 of the Supplemental Material [72]. We notice that the frequency response can be tuned by varying the sublattice offset. However, as we keep on increasing Δ, we notice that the second-order response starts to diminish. This is to be expected as in addition to a suppression coming from the energy denominators exemplified in Eq. (11), the wave-function overlap between the bands decreases and the bands become more decoupled with increasing Δ.

An important point to notice about the flat-flat contribution is that it indirectly depends on the presence of dispersive bands. The shift vector between two flat bands has a contribution from virtual transitions to dispersive bands as evident from the second term in Eq. (11) even though we are focusing here on direct flat-to-flat transitions. As a result, the number of dispersive bands also plays an important role in deciding the behavior of the shift vector originating from transitions between the two flat bands. In our simulations we found that, to achieve convergence of the second-order conductivity, it was necessary to include ten dispersive bands while evaluating the shift vector using the expression in Eq. (11) (where virtual transitions are captured by the second term).

We now focus on another contribution to second-order conductivity that comes from real transitions between a flat band and a dispersive band depicted by orange arrows in Fig. 2(a) (which we refer to as FD). In this case, the integrand

$\sum_{mn} f_{mn} R^{xxy}_{mn} \delta(\omega - \varepsilon_{mn})$ (we include those indices which account for transitions between flat and dispersive bands) is concentrated around the γ point in k space [Fig. 2(e)], and thus we observe a significant nonzero contribution only when the Fermi level lies between a flat band and a dispersive band.

Just as in the case of the flat-to-flat response in Fig. 2(b), we can similarly extract the θ-independent form of the photoresponse corresponding to flat-to-dispersive transitions. As expected from Eq. (11), the integrand R^{xxy}_{mn} decreases as $1/\varepsilon^2_{fd}$, where ε_{fd} is the gap between the flat band and the dispersive band. This gap shows a very strong dependence on twist angle θ as it increases sharply with the increase in mini-BZ size. The integral also carries an additional length-scale dependence. Hence, to present results in a twist-angle-independent manner, we rescale the response by a prefactor ε^2_{fd}/L_M, where L_M is the moiré length as shown in Fig. 2(c). Although the main plot shown in this figure was obtained for the twist angle $\theta = 0.8^\circ$, it looks quantitatively identical for all other twist angles near the magic angle. As evident from the behavior of the scaling factor ε^2_{fd}/L_M, the second-order conductivity is orders of magnitude larger for $\theta = 0.8^\circ$ in comparison to $\theta > 1^\circ$, and the peak value is approximately equal to 20 000 μA nm V^{-2} for this twist angle, which is an order of magnitude higher than that corresponding to the flat-to-flat transitions in Fig. 2(b). We also highlight that the largest response is seen at a frequency corresponding to that of a flat-to-dispersive band gap, $\omega = \varepsilon_{fd}$, but additional resonances occur at higher frequencies. We will explore these features in the following section.

Similar to the first contribution to the shift-current response, the second contribution arising from the flat-to-dispersive band transitions is influenced by the substrate properties. When the sublattice offset Δ is increased from 5 to 10 meV, we notice that the FD signal is shifted to a lower frequency and the peak becomes more pronounced as shown in Fig. S2(c) of the Supplemental Material [72]. This can be explained on the basis of the shift in band energies (Fig. S2(a) of the Supplemental Material [72]). An increased Δ increases the gap between flat bands but does not affect the dispersive bands much. As a result, the gap between flat and dispersive bands starts to decrease. A smaller value of the gap, ε_{fd}, shifts the peak to a lower frequency and also increases the value of the integrand, which scales as $1/\varepsilon_{fd}$ as mentioned earlier. However, if we increase the sublattice offset further, it suppresses the overlap between Bloch wave functions, as discussed previously in the context of flat-to-flat transitions, and the shift-current signal is diminished as shown in Fig. S2 of the Supplemental Material [72]. This shows that the sublattice offset can serve as an important knob to tune the optical response. Additionally, the direction of the current density and its relation to the polarization of the EM field can also be modified by changing the sublattice offset independently in two layers. As discussed in Sec. III D, the constraints on the second-order conductivity tensor are different for the $\Delta_1 = \Delta_2$ case and the $\Delta_1 \neq \Delta_2$ case. Here, in Figs. 2–4, we have considered $\Delta_1 = \Delta_2$, and thus the only nonzero components are $\sigma^y_{xx}, \sigma^y_{yy}, \sigma^y_{xy}, \sigma^x_{yx} \neq 0$, which can all be expressed in terms of σ^y_{xx} plotted in these figures. We also verified the relation between different elements as shown in Fig. S3 of the Supplemental Material [72]. However, for $\Delta_1 \neq \Delta_2$, there are two independent nonzero elements, which are shown in the lower panel of Fig. S3.

V. EFFECTS OF INTERACTIONS ON SHIFT-CURRENT RESPONSE

Next, we discuss how the shift-current response is modified by electron-electron interactions, which we incorporate by using the mean-field procedure described in Sec. III B. As shown in Fig. 1(b), one of the most prominent effects of interactions is the band flattening of the flat bands near the γ point causing a large enhancement of the density of states. Additionally, these interactions also affect the structure of Bloch wave functions in real space, which modifies the shift vector.

For the flat-to-flat contribution shown in the noninteracting case, we noticed that the σ^y_{xx} peak was significantly larger for fillings $\nu \approx 2$ [Fig. 2(b)]. We explained this behavior on the basis of a significant contribution from the extreme flat regions around the μ points, corresponding to the van Hove singularities, as depicted in Figs. 2(b) and 5(a). Upon increasing the filling further beyond these flat regions, the transitions to these states are Pauli blocked, and they no longer contribute to the optical response in the noninteracting case. However, when electron-electron interactions are included in the analysis, we notice that these flat regions around the μ point expand further in k space as shown in Fig. 3(a) until they span the whole mini BZ (when the γ point is locally flat). Now, these extremely flat regions can participate in band transitions even at higher fillings. It consequently affects the peaks at larger fillings, e.g., $|\nu| > 3$, which not only increase in strength but also shift in frequency and coincide with the peaks at fillings $|\nu| = 1.5, 2$, c.f. Fig. 3(b). This behavior clearly arises due to the increased density of states coming from Hartree band flattening that shifts van Hove singularity to higher fillings [cf. Supplemental Material Fig. S1(b) for a chemical level assignment for each filling]. Additionally, we also notice a change in the profile of the flat-to-dispersive contribution of the integrand $\sum_{mn} R^{xxy}_{mn} \delta(\omega - \varepsilon_{mn})$ along the γ-μ line which leads to an increased asymmetry in positive and negative regions of the mini BZ with increasing $|\nu|$ as depicted in the third column of Fig. 3(c), and hence an enhanced response.

These interaction-induced changes in band structure also affect the contribution coming from transitions between flat and dispersive bands. One obvious modification arises from the changes in band structure which are quite prominent around the γ point. This region was the hot spot for the FD contribution in the noninteracting case as discussed in Sec. IV and shown in Fig. 2(e). The Hartree corrections to the noninteracting Hamiltonian increase the gap at the γ points. This correction also results in an increased band flattening of dispersive bands, which in turn decreases the gap significantly in a large region of the mini BZ around the μ points as shown in Fig. 4(a).

These Hartree corrections to the band structure and Bloch wave functions also modify the shift-current integrand, R^{xxy}. Its momentum profile exhibits a significant increase in regions away from the γ point as shown in Figs. 4(d)–4(g) and 6(b). These factors give rise to some unexpected features in the second-order conductivity response. We can now observe a

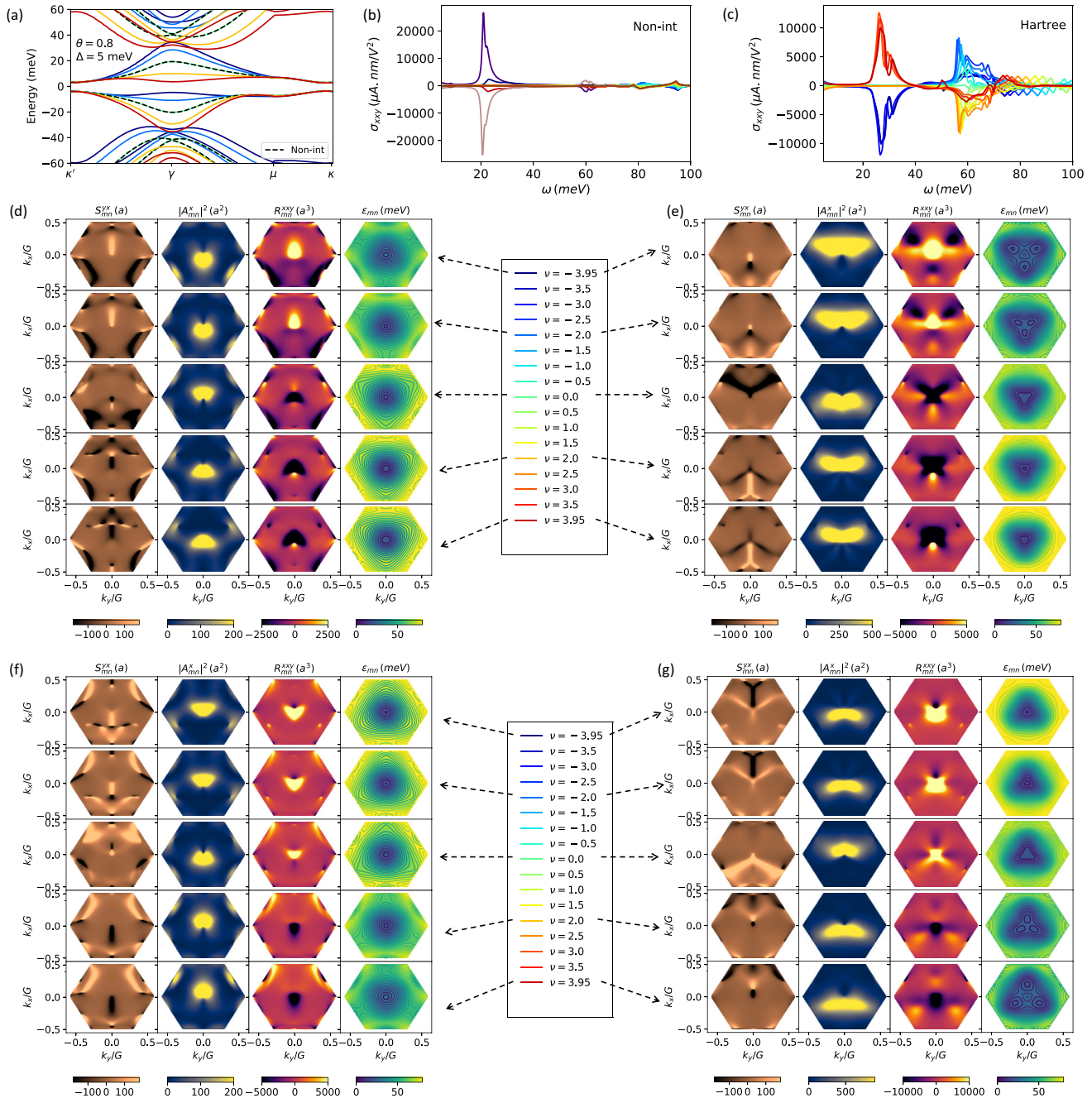

FIG. 4. Interaction-induced modification of band structure, second-order conductivity, shift vector, and interband Berry connection for flat-to-dispersive band transitions. (a) Band structure with Hartree corrections showing flat and dispersive bands, (b) FD contribution to shift-current conductivity for the noninteracting case, and (c) FD contribution when Hartree corrections are included. Note the appearance of additional peaks in (c) as compared with (b). (d)–(g) Shift vector S^{yx}_{mn}, interband Berry connection magnitude square, $|A^{x}_{mn}|^2$, the integrand R^{xxy}_{mn}, and energy contours for ε_{fd} in k space for the four FD transitions, where (d) and (e) represent transitions between the hole flat band and hole dispersive bands and (f) and (g) describe transitions between the electron flat band and the electron dispersive bands.

reasonably large contribution at fillings less than $|\nu| = 4$, which arises due to the spreading of R^{xxy}_{mn} in the mini BZ as shown in the bottom panel of Fig. 6(b).

Arguably, however, the most important role (at least experimentally) of these filling-dependent corrections is the appearance of new features in the second-order shift-current conductivity. Specifically, there is also a second peak, in Fig. 4(c) at $\omega \approx 60$ meV, which has the opposite sign to the peak at $\omega \approx 25$ meV. We attribute this second peak to transitions that involve van Hove singularity points of the flat band as their frequency is quite close to the energy gap around those k points. This is further substantiated by the

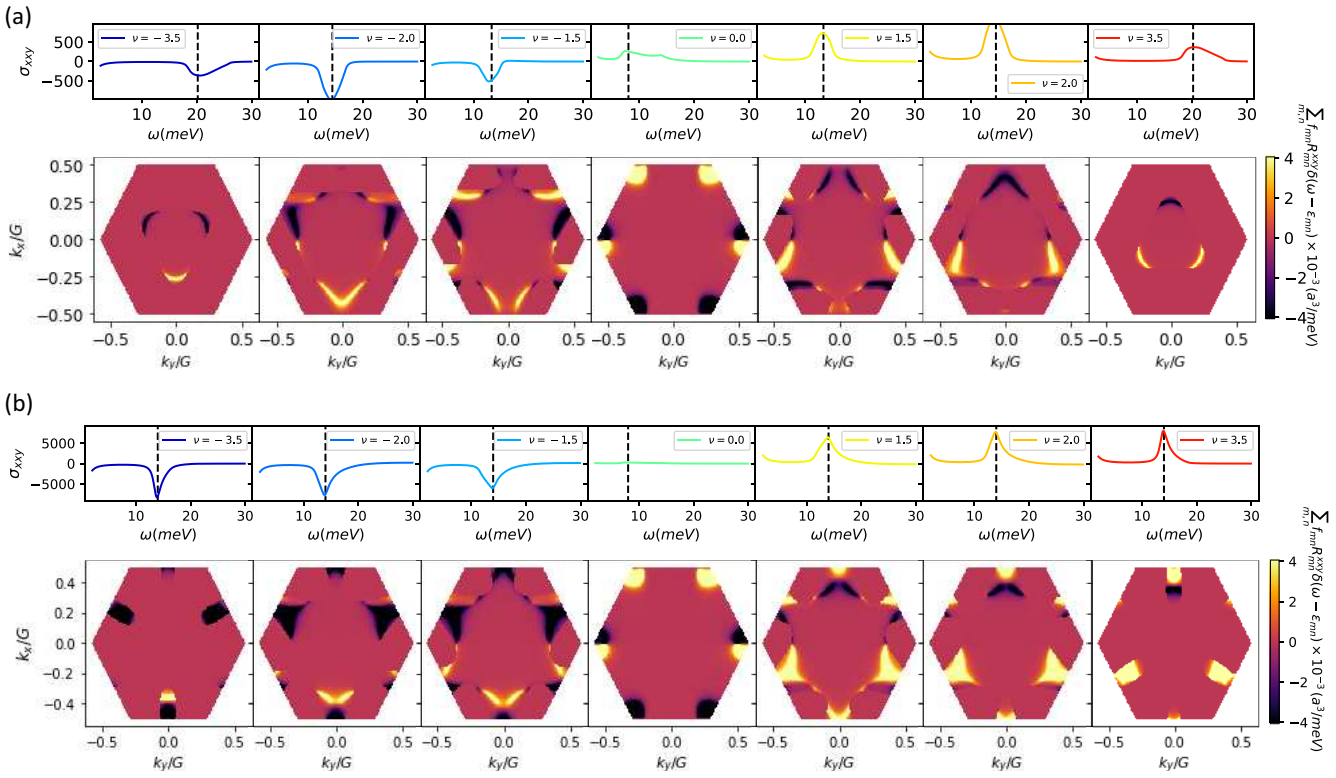

FIG. 5. Comparison between the momentum space profile of the FF contribution of shift-current conductivity for the noninteracting and interacting case at peak frequencies for different filling factors. The flat-to-flat band transition contribution to the peak of second-order conductivity from different k points within the mini BZ at different filling factors for the (a) noninteracting model and (b) interacting model with Hartree corrections. In each set of panels (consisting of an upper and a lower panel), the upper panel shows the variation of the shift-current conductivity with frequency at a given filling, and the lower panel shows the k-space profile of the shift-current integrand from Eq. (10) for the flat-to-flat band transitions at frequencies corresponding to the dashed line in the upper panel. We notice a significant increase in the contribution from the regions near the μ point which mainly arises from the band-flattening effect of interactions.

fact that the integrand in these regions is opposite to that of the contribution from the γ point as shown in Fig. 6(b) and the third column of Figs. 4(e) and 4(f). We argue that this enhanced response and the appearance of the second peak can act as a probe of interaction-induced changes to both the band structure and the quantum geometry. Most crucially, however, this additional peak occurs at frequencies that far exceed those characteristic frequencies of flat-to-flat band transitions (a few meVs), placing it more firmly in the characteristic range of optical experiments (tens of meVs).

VI. DISCUSSION

In this paper, we presented a detailed analysis of the shift-current response in TBG and investigated the role of twist angle, doping, encapsulation environment, and interactions in the shift-current response of twisted bilayer graphene. We identified two different contributions: one arising from the transitions between two flat bands and another from the transitions between a flat band and a dispersive band as shown in Fig. 1. In the absence of interactions, the first and second contributions result in a second-order conductivity with peak values of $\sim$1000 and $\sim$10 000 μA nm V^{-2}, respectively, with the typical frequency dependence tunable by changing the twist angle and the sublattice offset. This giant photoresponse arising from the nontrivial band topology of flat bands in TBG renders it an exceptional material for photovoltaic applications in the terahertz range. Additionally, we showed that interactions can significantly alter the photoresponse of TBG. This opens up a route for probing interaction-induced changes to band structure and quantum geometry with the help of optical probes.

Alongside the shift-current response, the circular photogalvanic effect (CPGE) and, generally, injection photocurrents also occur in materials with Dirac cone dispersions. The injection current emerges from the difference in group velocities between the original and excited bands and is proportional to the electronic relaxation time. It is usually the dominant second-order photocurrent response in Weyl semimetals [24,40]. It requires, however, circularly polarized light or tilted Dirac cones illuminated by linearly polarized light to be nonzero. Our work considered only the linear polarization response and ignored these additional terms, which we expect are either subleading in TBG or vanish by symmetry considerations. Specifically, for a two-dimensional system with C_{3z} symmetry, even the circular polarization cannot generate an in-plane injection current at normal incidence (see Ref. [82] and discussion in Appendix C of the Supplemental Material [72]). As such, unless C_{3z} symmetry is lifted, for example, by applying a strain (as recently shown in Ref. [83]) or by

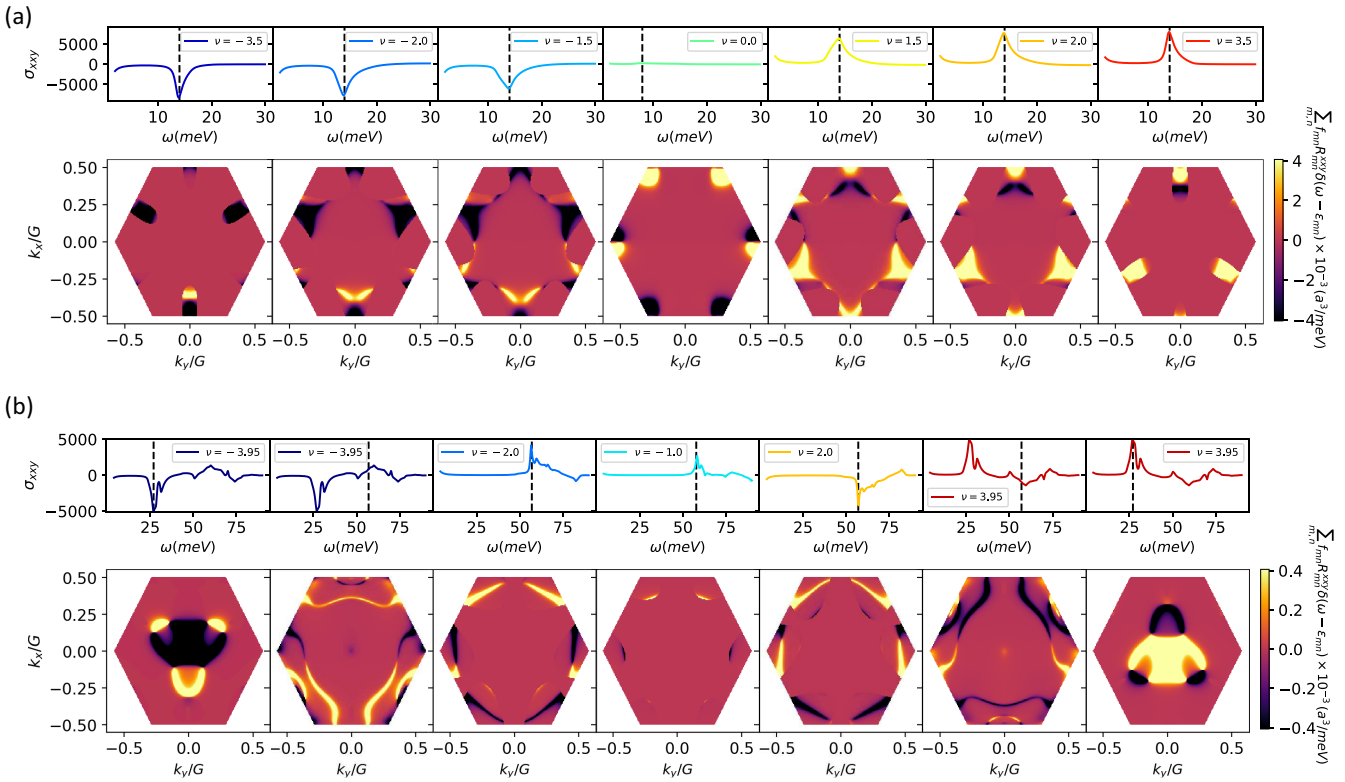

FIG. 6. Comparison between the momentum space profile of the FD contribution of shift-current conductivity for the noninteracting and interacting case at peak frequencies for different filling factors. The flat-to-dispersive band transition contribution to the peak of second-order conductivity from different k points within the mini BZ at different filling factors for the (a) noninteracting model and (b) interacting model with Hartree corrections. In each set of panels (consisting of an upper and a lower panel), the upper panel shows the variation of the shift-current conductivity with frequency at a given filling, and the lower panel shows the k-space profile of the shift-current integrand from Eq. (10) for the flat-to-dispersive band transitions at frequencies corresponding to the dashed line in the upper panel. We notice a significant increase in the contribution from the regions near the μ point which mainly arises from the band-flattening effect of interactions.

interactions [84–86] beyond the Hartree correction considered here, we expect the injection current to vanish under these conditions in TBG.

Another interesting aspect is the dependence of the shift vector on the nature of the perturbation, i.e., the momentum derivative of the excitation matrix phase [87]. It could be interesting to contrast this contribution to the shift current with currents induced by other nonequilibrium perturbations arising from coupling between EM fields and other degrees of freedom such as orbital or phononic degrees of freedom.

Furthermore, in this paper we mainly focused on the photoresponse originating from interband processes. However, if the spatial symmetry of the system is lowered further by breaking some mirror symmetries, we could also get a second-order contribution from intraband processes which are captured by the Berry curvature dipole [27]. Such semiclassical processes can be made to contribute to the nonlinear optical response by applying a strain as discussed in Refs. [36,88]. In TBG, we expect the strain-induced contribution to be of the same order of magnitude [51], and therefore it should not alter our results drastically.

Another interesting effect is the impact of valley polarization on the shift current and the photoresponse in general. Our shift-current expression considered in Eq. (10) has equal contributions from both valleys if the Dirac cones of the underlying graphene layers are not tilted. However, in addition to the shift-current contribution which comes with a Dirac-delta function, the second-order conductivity also has a contribution from the principal part as presented in Eq. (B22) of Appendix B of the Supplemental Material [72]. This contribution is equal and opposite to that from two valleys and hence can affect the shift-current response for a valley-polarized setup only. This valley dependence would be even more apparent for injection currents.

As pointed out earlier, the shift currents are a reflection of the quantum geometry of the electronic bands. The effect is also clearly related to the charge distribution of the Bloch wave functions in the moiré unit cell. Indeed, as argued in Sec. III B, different momentum states lead to a different spatial distribution of charge; for example, for flat bands, κ, κ'-point states give rise to charge buildup near AA sites, while γ-point states cause a buildup of charge in a ring surrounding AA sites. For the first dispersive bands, however, the relation flips: κ, κ'-point states give rise to charge buildup in a ring surrounding AA sites, while γ-point states lead to a charge buildup at the AA sites. We propose that the qualitatively sharp resonances seen in Fig. 4 correspond to the transitions from an AA charge profile to that of a ring surrounding the AA sites or vice versa, but the precise relation remains to be

explored (see Appendix D of the Supplemental Material [72] for further discussion). In future work, it would be fascinating to consider what additional effects emerge from these unusual rearrangements of the electronic probability density within the moiré unit cell.

ACKNOWLEDGMENTS

We thank Stevan Nadj-Perge for an earlier collaboration and useful discussions. We acknowledge support from the Institute of Quantum Information and Matter, an NSF Physics Frontiers Center funded by the Gordon and Betty Moore Foundation, the Packard Foundation, and the Simons Foundation. G.R. and S.C. are grateful for support from the U.S. Department of Energy, Office of Science, Basic Energy Sciences, under Award No. desc0019166. G.R. is also grateful to NSF DMR Grant No. 1839271. C.L. acknowledges support from the Gordon and Betty Moore Foundation through Grant No. GBMF8682.

[1] Y. Cao, V. Fatemi, A. Demir, S. Fang, S. L. Tomarken, J. Y. Luo, J. D. Sanchez-Yamagishi, K. Watanabe, T. Taniguchi, E. Kaxiras, R. C. Ashoori, and P. Jarillo-Herrero, Correlated insulator behaviour at half-filling in magic-angle graphene superlattices, Nature (London) **556**, 80 (2018).

[2] X. Lu, P. Stepanov, W. Yang, M. Xie, M. A. Aamir, I. Das, C. Urgell, K. Watanabe, T. Taniguchi, G. Zhang, A. Bachtold, A. H. MacDonald, and D. K. Efetov, Superconductors, orbital magnets and correlated states in magic-angle bilayer graphene, Nature (London) **574**, 653 (2019).

[3] M. Serlin, C. L. Tschirhart, H. Polshyn, Y. Zhang, J. Zhu, K. Watanabe, T. Taniguchi, L. Balents, and A. F. Young, Intrinsic quantized anomalous Hall effect in a moiré heterostructure, Science **367**, 900 (2020).

[4] A. L. Sharpe, E. J. Fox, A. W. Barnard, J. Finney, K. Watanabe, T. Taniguchi, M. A. Kastner, and D. Goldhaber-Gordon, Emergent ferromagnetism near three-quarters filling in twisted bilayer graphene, Science **365**, 605 (2019).

[5] Y. Cao, V. Fatemi, S. Fang, K. Watanabe, T. Taniguchi, E. Kaxiras, and P. Jarillo-Herrero, Unconventional superconductivity in magic-angle graphene superlattices, Nature (London) **556**, 43 (2018).

[6] M. Yankowitz, S. Chen, H. Polshyn, Y. Zhang, K. Watanabe, T. Taniguchi, D. Graf, A. F. Young, and C. R. Dean, Tuning superconductivity in twisted bilayer graphene, Science **363**, 1059 (2019).

[7] L. Balents, C. R. Dean, D. K. Efetov, and A. F. Young, Superconductivity and strong correlations in moiré flat bands, Nat. Phys. **16**, 725 (2020).

[8] U. Zondiner, A. Rozen, D. Rodan-Legrain, Y. Cao, R. Queiroz, T. Taniguchi, K. Watanabe, Y. Oreg, F. von Oppen, A. Stern, E. Berg, P. Jarillo-Herrero, and S. Ilani, Cascade of phase transitions and Dirac revivals in magic-angle graphene, Nature (London) **582**, 203 (2020).

[9] D. Wong, K. P Nuckolls, M. Oh, B. Lian, Y. Xie, S. Jeon, K. Watanabe, T. Taniguchi, B. A. Bernevig, and A. Yazdani, Cascade of electronic transitions in magic-angle twisted bilayer graphene, Nature (London) **582**, 198 (2020).

[10] D. Xiao, M.-C. Chang, and Q. Niu, Berry phase effects on electronic properties, Rev. Mod. Phys. **82**, 1959 (2010).

[11] T. Morimoto and N. Nagaosa, Topological nature of nonlinear optical effects in solids, Sci. Adv. **2**, e1501524 (2016).

[12] J. Ahn, G.-Y. Guo, and N. Nagaosa, Low-Frequency Divergence and Quantum Geometry of the Bulk Photovoltaic Effect in Topological Semimetals, Phys. Rev. X **10**, 041041 (2020).

[13] Q. Ma, A. G. Grushin, and K. S. Burch, Topology and geometry under the nonlinear electromagnetic spotlight, Nat. Mater. **20**, 1601 (2021).

[14] J. Orenstein, J. E. Moore, T. Morimoto, D. H. Torchinsky, J. W. Harter, and D. Hsieh, Topology and symmetry of quantum materials via nonlinear optical responses, Annu. Rev. Condens. Matter Phys. **12**, 247 (2021).

[15] J. Ahn, G.-Y. Guo, N. Nagaosa, and A. Vishwanath, Riemannian geometry of resonant optical responses, Nat. Phys. (2021).

[16] G. E. Topp, C. J. Eckhardt, D. M. Kennes, M. A. Sentef, and P. Törmä, Light-matter coupling and quantum geometry in moiré materials, Phys. Rev. B **104**, 064306 (2021).

[17] G. B. Osterhoudt, L. K. Diebel, M. J. Gray, X. Yang, J. Stanco, X. Huang, B. Shen, N. Ni, P. J. W. Moll, Y. Ran, and K. S. Burch, Colossal mid-infrared bulk photovoltaic effect in a type-I Weyl semimetal, Nat. Mater. **18**, 471 (2019).

[18] C.-K. Chan, P. A. Lee, K. S. Burch, J. H. Han, and Y. Ran, When Chiral Photons Meet Chiral Fermions: Photoinduced Anomalous Hall Effects in Weyl Semimetals, Phys. Rev. Lett. **116**, 026805 (2016).

[19] X. Yang, K. Burch, and Y. Ran, Divergent bulk photovoltaic effect in Weyl semimetals, arXiv:1712.09363 [cond-mat.mes-hall].

[20] H. Isobe, S.-Y. Xu, and L. Fu, High-frequency rectification via chiral Bloch electrons, Sci. Adv. **6**, eaay2497 (2020).

[21] F. D. M. Haldane, Model for a Quantum Hall Effect without Landau Levels: Condensed-Matter Realization of the "Parity Anomaly", Phys. Rev. Lett. **61**, 2015 (1988).

[22] S.-Y. Xu, Q. Ma, H. Shen, V. Fatemi, S. Wu, T.-R. Chang, G. Chang, A. M. M. Valdivia, C.-K. Chan, Q. D. Gibson, J. Zhou, Z. Liu, K. Watanabe, T. Taniguchi, H. Lin, R. J. Cava, L. Fu, N. Gedik, and P. Jarillo-Herrero, Electrically switchable Berry curvature dipole in the monolayer topological insulator WTe_2, Nat. Phys. **14**, 900 (2018).

[23] L. Wu, S. Patankar, T. Morimoto, N. L. Nair, E. Thewalt, A. Little, J. G. Analytis, J. E. Moore, and J. Orenstein, Giant anisotropic nonlinear optical response in transition metal monopnictide Weyl semimetals, Nat. Phys. **13**, 350 (2017).

[24] F. de Juan, A. G. Grushin, T. Morimoto, and J. E. Moore, Quantized circular photogalvanic effect in Weyl semimetals, Nat. Commun. **8**, 15995 (2017).

[25] H. Wang and X. Qian, Ferroicity-driven nonlinear photocurrent switching in time-reversal invariant ferroic materials, Sci. Adv. **5**, eaav9743 (2019).

[26] J. E. Moore and J. Orenstein, Confinement-Induced Berry Phase and Helicity-Dependent Photocurrents, Phys. Rev. Lett. **105**, 026805 (2010).

[27] I. Sodemann and L. Fu, Quantum Nonlinear Hall Effect Induced by Berry Curvature Dipole in Time-Reversal Invariant Materials, Phys. Rev. Lett. **115**, 216806 (2015).

[28] S. M. Young and A. M. Rappe, First Principles Calculation of the Shift Current Photovoltaic Effect in Ferroelectrics, Phys. Rev. Lett. **109**, 116601 (2012).

[29] T. Rangel, B. M. Fregoso, B. S. Mendoza, T. Morimoto, J. E. Moore, and J. B. Neaton, Large Bulk Photovoltaic Effect and Spontaneous Polarization of Single-Layer Monochalcogenides, Phys. Rev. Lett. **119**, 067402 (2017).

[30] L. Z. Tan and A. M. Rappe, Enhancement of the Bulk Photovoltaic Effect in Topological Insulators, Phys. Rev. Lett. **116**, 237402 (2016).

[31] L. Z. Tan, F. Zheng, S. M. Young, F. Wang, S. Liu, and A. M. Rappe, Shift current bulk photovoltaic effect in polar materials-hybrid and oxide perovskites and beyond, npj Comput. Mater. **2**, 16026 (2016).

[32] A. M. Cook, B. M. Fregoso, F. De Juan, S. Coh, and J. E. Moore, Design principles for shift current photovoltaics, Nat. Commun. **8**, 14176 (2017).

[33] Z.-S. Liao, H.-H. Zhang, and Z. Yan, Nonlinear Hall effect in two-dimensional class-AI metals, Phys. Rev. B **103**, 235151 (2021).

[34] C.-P. Zhang, J. Xiao, B. T. Zhou, J.-X. Hu, Y.-M. Xie, B. Yan, and K. T. Law, Giant nonlinear Hall effect in strained twisted bilayer graphene, arXiv:2010.08333 [cond-mat.mes-hall].

[35] C. Ortix, Nonlinear Hall effect with time-reversal symmetry: Theory and material realizations, Adv. Quantum Technol. **4**, 2100056 (2021).

[36] P. A. Pantaleón, T. Low, and F. Guinea, Tunable large Berry dipole in strained twisted bilayer graphene, Phys. Rev. B **103**, 205403 (2021).

[37] Z. He and H. Weng, Giant nonlinear Hall effect in twisted bilayer WTe_2, npj Quantum Mater. **6**, 101 (2021).

[38] N. Ogawa, M. Sotome, Y. Kaneko, M. Ogino, and Y. Tokura, Shift current in the ferroelectric semiconductor SbSI, Phys. Rev. B **96**, 241203(R) (2017).

[39] P. Hosur, Circular photogalvanic effect on topological insulator surfaces: Berry-curvature-dependent response, Phys. Rev. B **83**, 035309 (2011).

[40] C.-K. Chan, N. H. Lindner, G. Refael, and P. A. Lee, Photocurrents in Weyl semimetals, Phys. Rev. B **95**, 041104(R) (2017).

[41] R. von Baltz and W. Kraut, Theory of the bulk photovoltaic effect in pure crystals, Phys. Rev. B **23**, 5590 (1981).

[42] V. I. Belinicher, E. L. Ivchenko, and B. I. Sturman, Kinetic theory of the displacement photovoltaic effect in piezoelectrics, Zh. Eksp. Teor. Fiz. **83**, 649 (1982) [Sov. Phys. JETP **56**, 359 (1982)].

[43] J. E. Sipe and A. I. Shkrebtii, Second-order optical response in semiconductors, Phys. Rev. B **61**, 5337 (2000).

[44] B. I. Sturman, Ballistic and shift currents in the bulk photovoltaic effect theory, Phys.-Usp. **63**, 407 (2020).

[45] T. Holder, D. Kaplan, and B. Yan, Consequences of time-reversal-symmetry breaking in the light-matter interaction: Berry curvature, quantum metric, and diabatic motion, Phys. Rev. Research **2**, 033100 (2020).

[46] Y. Xiong, L.-K. Shi, and J. C. W. Song, Atomic configuration controlled photocurrent in van der Waals homostructures, 2D Mater. **8**, 035008 (2021).

[47] A. M. Schankler, L. Gao, and A. M. Rappe, Large bulk piezophotovoltaic effect of monolayer $2H$-MoS_2, J. Phys. Chem. Lett. **12**, 1244 (2021).

[48] H. Ai, Y. Kong, D. Liu, F. Li, J. Geng, S. Wang, K. H. Lo, and H. Pan, $1T'''$ transition-metal dichalcogenides: Strong bulk photovoltaic effect for enhanced solar-power harvesting, J. Phys. Chem. C **124**, 11221 (2020).

[49] H. Xu, H. Wang, J. Zhou, Y. Guo, J. Kong, and J. Li, Colossal switchable photocurrents in topological Janus transition metal dichalcogenides, npj Comput. Mater. **7**, 31 (2021).

[50] F. Xie, Z. Song, B. Lian, and B. A. Bernevig, Topology-Bounded Superfluid Weight in Twisted Bilayer Graphene, Phys. Rev. Lett. **124**, 167002 (2020).

[51] D. Kaplan, T. Holder, and B. Yan, Momentum shift current at terahertz frequencies in twisted bilayer graphene, arXiv:2101.07539 [cond-mat.mes-hall].

[52] J. Liu and X. Dai, Anomalous Hall effect, magneto-optical properties, and nonlinear optical properties of twisted graphene systems, npj Comput. Mater. **6**, 57 (2020).

[53] F. Guinea and N. R. Walet, Electrostatic effects, band distortions, and superconductivity in twisted graphene bilayers, Proc. Natl. Acad. Sci. USA **115**, 13174 (2018).

[54] Z. A. H. Goodwin, V. Vitale, X. Liang, A. A. Mostofi, and J. Lischner, Hartree theory calculations of quasiparticle properties in twisted bilayer graphene, Electron. Struct. **2**, 034001 (2020).

[55] T. Cea, N. R. Walet, and F. Guinea, Electronic band structure and pinning of Fermi energy to Van Hove singularities in twisted bilayer graphene: A self-consistent approach, Phys. Rev. B **100**, 205113 (2019).

[56] T. Cea and F. Guinea, Band structure and insulating states driven by Coulomb interaction in twisted bilayer graphene, Phys. Rev. B **102**, 045107 (2020).

[57] L. Rademaker, D. A. Abanin, and P. Mellado, Charge smoothening and band flattening due to Hartree corrections in twisted bilayer graphene, Phys. Rev. B **100**, 205114 (2019).

[58] N. Bultinck, E. Khalaf, S. Liu, S. Chatterjee, A. Vishwanath, and M. P. Zaletel, Ground State and Hidden Symmetry of Magic-Angle Graphene at Even Integer Filling, Phys. Rev. X **10**, 031034 (2020).

[59] A. Kerelsky, L. J. McGilly, D. M. Kennes, L. Xian, M. Yankowitz, S. Chen, K. Watanabe, T. Taniguchi, J. Hone, C. Dean, A. Rubio, and A. N. Pasupathy, Maximized electron interactions at the magic angle in twisted bilayer graphene, Nature (London) **572**, 95 (2019).

[60] Y. Choi, J. Kemmer, Y. Peng, A. Thomson, H. Arora, R. Polski, Y. Zhang, H. Ren, J. Alicea, G. Refael, F. von Oppen, K. Watanabe, T. Taniguchi, and S. Nadj-Perge, Electronic correlations in twisted bilayer graphene near the magic angle, Nat. Phys. **15**, 1174 (2019).

[61] Y. Choi, H. Kim, C. Lewandowski, Y. Peng, A. Thomson, R. Polski, Y. Zhang, K. Watanabe, T. Taniguchi, J. Alicea, and S. Nadj-Perge, Interaction-driven band flattening and correlated phases in twisted bilayer graphene, Nat. Phys. **17**, 1375 (2021).

[62] Y. Choi, H. Kim, Y. Peng, A. Thomson, C. Lewandowski, R. Polski, Y. Zhang, H. S. Arora, K. Watanabe, T. Taniguchi, J. Alicea, and S. Nadj-Perge, Correlation-driven topological phases in magic-angle twisted bilayer graphene, Nature (London) **589**, 536 (2021).

[63] H. Kim, Y. Choi, C. Lewandowski, A. Thomson, Y. Zhang, R. Polski, K. Watanabe, T. Taniguchi, J. Alicea, and S. Nadj-Perge, Spectroscopic signatures of strong correlations and unconventional superconductivity in twisted trilayer graphene, arXiv:2109.12127 [cond-mat.mes-hall].

[64] A. Rozen, J. M. Park, U. Zondiner, Y. Cao, D. Rodan-Legrain, T. Taniguchi, K. Watanabe, Y. Oreg, A. Stern, E. Berg, P. Jarillo-Herrero, and S. Ilani, Entropic evidence for a Pomeranchuk effect in magic-angle graphene, Nature (London) **592**, 214 (2021).

[65] T. Morimoto, S. Zhong, J. Orenstein, and J. E. Moore, Semiclassical theory of nonlinear magneto-optical responses with applications to topological Dirac/Weyl semimetals, Phys. Rev. B **94**, 245121 (2016).

[66] M. Koshino, N. F. Q. Yuan, T. Koretsune, M. Ochi, K. Kuroki, and L. Fu, Maximally Localized Wannier Orbitals and the Extended Hubbard Model for Twisted Bilayer Graphene, Phys. Rev. X **8**, 031087 (2018).

[67] R. Bistritzer and A. H. MacDonald, Moiré bands in twisted double-layer graphene, Proc. Natl. Acad. Sci. USA **108**, 12233 (2011).

[68] J. M. B. Lopes dos Santos, N. M. R. Peres, and A. H. Castro Neto, Graphene Bilayer with a Twist: Electronic Structure, Phys. Rev. Lett. **99**, 256802 (2007).

[69] S. Carr, S. Fang, Z. Zhu, and E. Kaxiras, Exact continuum model for low-energy electronic states of twisted bilayer graphene, Phys. Rev. Research **1**, 013001 (2019).

[70] M. Xie and A. H. MacDonald, Nature of the Correlated Insulator States in Twisted Bilayer Graphene, Phys. Rev. Lett. **124**, 097601 (2020).

[71] E. Khalaf, S. Chatterjee, N. Bultinck, M. P. Zaletel, and A. Vishwanath, Charged skyrmions and topological origin of superconductivity in magic-angle graphene, Sci. Adv. **7**, eabf5299 (2021).

[72] See Supplemental Material at http://link.aps.org/supplemental/10.1103/PhysRevResearch.4.013164 for a description of the methods used.

[73] M. Xie and A. H. MacDonald, Weak-Field Hall Resistivity and Spin-Valley Flavor Symmetry Breaking in Magic-Angle Twisted Bilayer Graphene, Phys. Rev. Lett. **127**, 196401 (2021).

[74] L. Klebl, Z. A. H. Goodwin, A. A. Mostofi, D. M. Kennes, and J. Lischner, Importance of long-ranged electron-electron interactions for the magnetic phase diagram of twisted bilayer graphene, Phys. Rev. B **103**, 195127 (2021).

[75] C. Lewandowski, S. Nadj-Perge, and D. Chowdhury, Does filling-dependent band renormalization aid pairing in twisted bilayer graphene? npj Quantum Mater. **6**, 82 (2021).

[76] T. Cea and F. Guinea, Coulomb interaction, phonons, and superconductivity in twisted bilayer graphene, Proc. Natl. Acad. Sci. USA **118**, e2107874118 (2021).

[77] W. Qin, B. Zou, and A. H. MacDonald, Critical magnetic fields and electron-pairing in magic-angle twisted bilayer graphene, arXiv:2102.10504 [cond-mat.supr-con].

[78] B. M. Fregoso, T. Morimoto, and J. E. Moore, Quantitative relationship between polarization differences and the zone-averaged shift photocurrent, Phys. Rev. B **96**, 075421 (2017).

[79] D. E. Parker, T. Morimoto, J. Orenstein, and J. E. Moore, Diagrammatic approach to nonlinear optical response with application to Weyl semimetals, Phys. Rev. B **99**, 045121 (2019).

[80] Y. Zhang, H. Ishizuka, J. van den Brink, C. Felser, B. Yan, and N. Nagaosa, Photogalvanic effect in Weyl semimetals from first principles, Phys. Rev. B **97**, 241118(R) (2018).

[81] V. I. Belinicher and B. I. Sturman, The photogalvanic effect in media lacking a center of symmetry, Sov. Phys.-Usp. **23**, 199 (1980).

[82] M. S. Dresselhaus, G. Dresselhaus, and A. Jorio, *Group Theory: Application to the Physics of Condensed Matter* (Springer, New York, 2007).

[83] A. Arora, J. F. Kong, and J. C. W. Song, Strain-induced large injection current in twisted bilayer graphene, Phys. Rev. B **104**, L241404 (2021).

[84] R. M. Fernandes and J. W. F. Venderbos, Nematicity with a twist: Rotational symmetry breaking in a moiré superlattice, Sci. Adv. **6**, eaba8834 (2020).

[85] J. Liu and X. Dai, Theories for the correlated insulating states and quantum anomalous Hall effect phenomena in twisted bilayer graphene, Phys. Rev. B **103**, 035427 (2021).

[86] S. Liu, E. Khalaf, J. Y. Lee, and A. Vishwanath, Nematic topological semimetal and insulator in magic-angle bilayer graphene at charge neutrality, Phys. Rev. Research **3**, 013033 (2021).

[87] S. Chaudhary, M. Endres, and G. Refael, Berry electrodynamics: Anomalous drift and pumping from a time-dependent Berry connection, Phys. Rev. B **98**, 064310 (2018).

[88] R. Battilomo, N. Scopigno, and C. Ortix, Berry Curvature Dipole in Strained Graphene: A Fermi Surface Warping Effect, Phys. Rev. Lett. **123**, 196403 (2019).